ELSEVIER

Ultramicroscopy 88 (2001) 33–49

ultramicroscopy

www.elsevier.nl/locate/ultramic

Optimization of scanning transmission X-ray microscopy for the identification and quantitation of reinforcing particles in polyurethanes

A.P. Hitchcock[a,*], I. Koprinarov[a], T. Tyliszczak[a], E.G. Rightor[b], G.E. Mitchell[b], M.T. Dineen[b], F. Hayes[b], W. Lidy[c,1], R.D. Priester[c], S.G. Urquhart[d,2], A.P. Smith[d], H. Ade[d]

[a] *Brockhouse Institute for Materials Research, McMaster University, 1180 Main Street West, Hamilton, ON, Canada*
[b] *Dow Chemical, 1897 Building, Midland, MI 48667, USA*
[c] *Dow Chemical, Building B-1608, 2301 N. Brazosport Blvd. Freeport, TX 77541, USA*
[d] *Department of Physics, North Carolina State University, Raleigh, NC 27695, USA*

Received 2 May 2000; received in revised form 13 October 2000

Abstract

The morphology, size distributions, spatial distributions, and quantitative chemical compositions of co-polymer polyol-reinforcing particles in a polyurethane have been investigated with scanning transmission X-ray microscopy (STXM). A detailed discussion of microscope operating procedures is presented and ways to avoid potential artifacts are discussed. Images at selected photon energies in the C 1s, N 1s and O 1s regions allow unambiguous identification of styrene–acrylonitrile-based (SAN) copolymer and polyisocyanate polyaddition product-based (PIPA) reinforcing particles down to particle sizes at the limit of the spatial resolution (50 nm). Quantitative analysis of the chemical composition of individual reinforcing particles is achieved by fitting C 1s spectra to linear combinations of reference spectra. Regression analyses of sequences of images recorded through the chemically sensitive ranges of the C 1s, N 1s and O 1s spectra are used to generate quantitative compositional maps, which provide a fast and effective means of investigating compositional distributions over a large number of reinforcing particles. The size distribution of all particles determined by STXM is shown to be similar to that determined by TEM. The size distributions of each type of reinforcing particle, which differ considerably, were obtained by analysis of STXM images at chemically selective energies.

Keywords: X-ray microscopy; Polymers; Quantitative chemical mapping; Particle size distributions

1. Introduction

Soft X-ray spectromicroscopy is a powerful tool for chemical analysis of polymer microstructure. In this study, we demonstrate some of its capabilities – in particular, qualitative identification, quantitative chemical analysis, and spatial

*Corresponding author. Tel.: +1-905-525-9140 × 24749; fax: +1-905-521-2273.
E-mail address: aph@mcmaster.ca (A.P. Hitchcock).
[1] Dow Chemical, retired
[2] Current Address: Department of Chemistry, University of Saskatchewan, Saskatoon, SK, Canada S7N 5C9.

0304-3991/01/$ - see front matter
PII: S0304-3991(00)00113-3

metrology of reinforcing particles. In many practical applications the intrinsic chemical or mechanical properties of a polymer are modified in various ways through the use of reinforcing particles. In this case, the system investigated is a polyurethane containing two different types of copolymer polyol reinforcing particles.

Polyurethane polymers, in the form of free-rise or molded foams, are widely used in the automotive and furnishings industries. In order to make foams with higher hardness several different strategies are presently employed [1]. Copolymer polyol (CPP) particles, which are dispersions of polymer particles in polyether polyol, inorganic fibers, and low molecular weight cross-linker polyols, are preferred for stiffening slabstock foams which are made in long, continuous blocks or buns. In order to understand how reinforcing particles like co-polymer polyols affect mechanical properties such as elastic modulus, tear strength and resiliency, and in order to develop improved CPP substances, it is important to have analytical techniques which can probe the morphology and chemistry at the required spatial scale. While traditional chemical spectroscopies such as infrared or NMR are excellent at chemical characterization, they do not have adequate spatial resolution to address questions relating to the submicron composition of polymer blends containing reinforcing particles. Analytical transmission and scanning transmission electron microscopy (TEM/STEM) have superb spatial resolution and can provide useful polymer microanalysis when performed with care [2] but in most cases the high-energy electron beam causes too much radiation damage for detailed spectroscopic studies of the composition of small radiation-sensitive polymer phases. Also, on account of the lower energy resolution of analytical TEM/STEM using electron energy loss spectroscopy (EELS) [2,3], the ability to differentiate similar chemical species is not as good as synchrotron-based X-ray microscopy. Overall, NEXAFS microscopy performed on a high-resolution synchrotron beamline provides superior *chemical* contrast relative to TEM-EELS.

Over the past decade analytical soft X-ray microscopy has developed into a useful tool for characterizing soft materials such as polymers [4–7], as well as environmental and biological samples [8]. The variant used in this work, scanning transmission X-ray microscopy (STXM) [9–14] provides near-edge X-ray absorption spectra (NEXAFS) with $\sim$0.1 eV energy resolution, which provides quite good chemical analysis. The spatial resolution is of the order of 50 nm, adequate for studies of many reinforcing particle systems, including CPP particles in polyurethanes. While there is some radiation damage, particularly to the dominant aliphatic polyether or soft segment component, the damage rate is much lower than in electron microscopy studies of the same materials. This is consistent with a recent study of polyethylene terephthalate in which damage rates of X-ray and electron microscopy were compared quantitatively [14]. Recent related studies that describe complementary aspects of the application of NEXAFS microscopy to polymers include: spectroscopic investigations to develop the conceptual understanding of the origin of spectral features [5–7,16–19]; a systematic approach to quantitation through comparison to model polymer reference standards [19,20]; quantitative studies of urea and urethane (carbamate) composition in model homogeneous [19–21], and typical heterogeneous, phase segregated polyurethanes [22,23]; analysis of the orientation of polymer chains and functional groups using the polarization dependence of images and spectra [4,7].

In this work, scanning transmission X-ray microscopy has been used to study a polyurethane in which two types of copolymer polyol (CPP) reinforcing particles were used simultaneously. The polyurethane matrix is a high molecular weight polypropylene oxide (PPO) cross-linked with toluene diisocyanate (TDI). One CPP is poly(styrene-*co*-acrylonitrile) (symbolized here as SAN), and the other is an aromatic-carbamate rich *p*oly-*i*socyanate *p*oly-*a*ddition product (symbolized here as PIPA), derived from methylene diisocyanate (MDI) [24–26]. Both species were formed and dispersed in the polyether polyol component of the polyurethane formulations. The two types of particles are indistinguishable when an unstained sample is viewed in a transmission electron

microscope (TEM). In this study, STXM spectroscopy, imaging, and analysis procedures are developed which optimize the ability to distinguish and quantitatively analyze these two CPP particle types. The distributions of the sizes of the PIPA and SAN particles have been measured and compared to the average particle size distribution determined from transmission electron microscopy (TEM). The composition of the SAN and PIPA CPP particles has also been analyzed, both on a particle-by-particle basis, and through the use of compositional maps derived from image sequences [27].

2. Experimental

Thin sections of the specimens were prepared by cryo-microtoming plaques of the slabstock polyurethane at -120°C using a Reichert-Jung FC4E microtome. The plaques were made according to a procedure described earlier [1]. Sections were transferred dry to uncoated copper grids using an eyelash. Typical sections were judged to be 100 nm thick based on the interference colors of the sections on the knife edge. A JEOL 2000FX ATEM was used to examine unstained samples. When grids were studied by TEM to examine the morphology, radiation-induced spectroscopic changes were noted by STXM. Thus, the sections analyzed by STXM in this work were not previewed by TEM to avoid radiation damage artifacts.

C 1s images and NEXAFS spectra were recorded with the Stony Brook STXM at the X-1A beamline of the National Synchrotron Light Source (NSLS) [9–11]. C 1s, N 1s and O 1s images and NEXAFS spectra were recorded with the beamline 7.0 STXM at the Advanced Light Source (ALS) [12–14]. The principles and experimental details of the X-ray optics used in scanning transmission X-ray microscopy have been described in detail elsewhere [8,9]. Briefly, monochromated undulator radiation illuminates a Fresnel zone plate, which has a first-order focal position defined by $f = D\delta_{rN}/m\lambda$, where D is the zone plate diameter, δ_{rN} is the width of the outermost zone, m is the order of the zone plate employed, and λ is the X-ray wavelength (see Fig. 1). The diffraction limited resolution is given by $1.22\delta_{rN}/m$. An image is generated by monitoring the X-ray signal transmitted through a thin section of a specimen as it is raster-scanned at the focus of the zone plate. For these measurements the spatial resolution of the NSLS microscope was about 60 nm (Raleigh criterion) and the energy resolution was ~200 meV (the NSLS-based results reported herein were obtained during the commissioning of a new monochromator which now provides ~100 meV resolution). Measurements made with the ALS microscope provided higher energy resolution (~100 meV) but significantly lower spatial resolution (~100 nm) on account of mechanical vibration and limitations of the X-ray optics.

Point spectra of the CPP particles acquired with dwell times at each energy of <0.1 s at NSLS did not appear to be noticeably affected by radiation damage, although longer dwells were observed to damage the polyether matrix. Mass loss in the polyether-rich matrix occurs with a critical dose (defined as the dose which produces a $1/e$ decrease in the intensity of a specified spectral feature) which is ~60 times smaller than that for poly (ethylene terephthalate) [15]. The carbonyl group of the PIPA particles exhibits spectral changes with a critical dose that is ~15 times smaller than that for PET [28]. At the ALS the undulator gap must be scanned synchronously with the photon energy on account of the narrow undulator

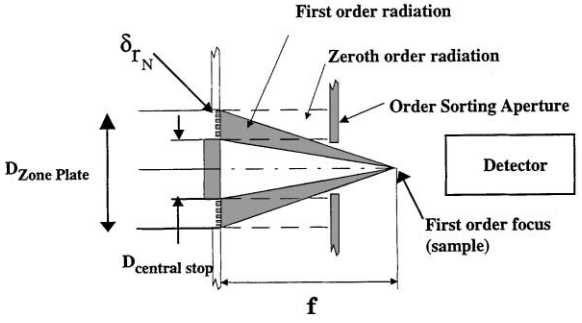

Fig. 1. Schematic of Fresnel zone plate focusing used in scanning transmission X-ray microscopy. δ_{rN} is the width of the outermost zone, and f is the focal length of the first-order diffraction spot.

spectral output, whereas full range NEXAFS spectra at the NSLS are acquired without changing the undulator gap. A mechanical shutter is used to block unwanted radiation during the change of monochromator energy and undulator gap, but the shutter has an uncertainly in its opening time of the order of 100 ms. Thus, for practical reasons, acquisition of point spectra at the ALS microscope is relatively slow – the minimum sampling period is about 1 s – and typically some X-ray flux hits the sample for between 0.3 and 0.5 s/energy point. In contrast point spectra at the NSLS are acquired with 20–60 ms/energy point since the undulator gap is not changed. The long sampling period combined with the $\sim 10\times$ higher flux at ALS relative to NSLS lead to significant beam damage over the course of acquiring a NEXAFS spectrum in point spectral mode at the ALS (when the focused X-ray beam is used). In order to obtain meaningful spectra with negligible radiation damage, the ALS microscope routinely uses sequences of images with short dwell times (0.2–0.4 ms per pixel) and a fine energy spacing. Subsequent post-processing aligns these images, then extracts spectra at any subset of pixels in the sampled region. Image alignment is necessary to correct for drifts of the field of view associated with lateral shifts in the position of the Fresnel zone plate focusing optical element as its *z*-position is scanned to retain focus with changing photon energy (wavelength). The software for image sequence acquisition at NSLS, and the subsequent analysis of the data (sometimes called 'stacks') was developed by Chris Jacobsen [27]. In addition to curve fit analysis of point spectra, we have also used newly developed procedures [29] to generate quantitative composition maps by a linear regression analysis of the spectrum at each pixel in an image sequence.

In order to obtain the most reliable quantitative analysis using STXM it is important to understand, monitor, and minimize a number of sources of systematic error. On the *instrumental side*, this includes factors such as detector non-linearity, spectral purity of the incident radiation, and the spatial profile of the zone plate focused beam [14]. Regarding detector linearity, the NSLS microscope uses a gas proportional counter operating in pulse counting mode which is linear to $\sim$1 MHz, with an efficiency of $\sim$15% and negligible dark count. The ALS microscope uses a phosphor (polycrystalline GdO_2S_2 : Tb, recently converted to a single-crystal yttrium aluminum phosphide) to convert X-rays to visible photons which are then detected in pulse mode with a high performance photomultiplier tube (Hammamatsu 647P). The overall system in the ALS microscope has a linear response up to 25 MHz, a measured efficiency of 30% at the C 1s edge, and a dark count of less that 200 Hz, which is negligible relative to the typical detected incident flux signal of 5–15 MHz.

With regard to spectral purity, the NSLS microscope is equipped with a two-mirror order suppression device which reduces higher orders to less than 1% [30]. Currently, ALS beamline 7.0 does not have a tunable order-sorting device but Ni coatings on mirrors provide an effective means to damp higher-order photons above 850 eV. Photoemission studies on this line indicate that the light incident on the zone plate has $\sim$4.5% second order and $\sim$1% third order at 300 eV. These levels are reduced to 0.6% and 0.5%, respectively if a 160 nm Ti filter foil is placed in the beam; however, the Ti filter was not incorporated in the beamline when these measurements were made. At the time of these experiments, the usable linear optical density range was limited to OD values of less than 3 at the ALS microscope, whereas, in CO_2 gas, linear optical density response up to 7 has been observed with the NSLS microscope when the order sorting mirrors have been tuned carefully.

The profile of the X-rays that impinge on the sample to generate the transmitted signal has a number of components: the desired focused spot from first-order diffraction, the portion of the second-order diffraction that passes through the order sorting aperture, un-diffracted beam in cases where the central stop is not sufficiently opaque, and a diffuse scattering halo due to imperfections in the placement and profile of the zone plate zones. The superimposition of light from all sources other than the first-order focused spot gives rise to a broad, structured distribution many times the focal spot size – the so-called "halo". Under most favorable conditions, the integrated

intensity of all of the halo (i.e. everything outside the focal spot) is $<1\%$ of the focused beam. If the order-sorting aperture (OSA) and central stop of the zone plate are not aligned, then un-diffracted beam which passes around the central stop will increase the halo intensity. Under certain circumstances, the halo can give rise to signal artifacts which can affect the accuracy of quantitative analysis. For example, when the sample under study is a strongly absorbing species embedded in a more transparent matrix (e.g. carbon black in a polymer matrix), then 1–2% of transmitted light in the halo region becomes a significant fraction of the observed signal. In such cases, the halo signal limits the maximum optical density one can observe without effective absorption saturation, and the X-ray absorption signal reflects the matrix as well as the dense embedded species. Clearly careful tuning of the microscope is an important factor in producing accurate results.

On the *operational side*, one must use acquisition techniques which provide meaningful incident flux (I_0) signals, good energy calibration, and one must monitor the extent of radiation damage. At both the NSLS and ALS microscopes the I_0 signal used to generate optical densities is recorded before or after the actual measurement. It is necessary to use this approach in order to have the same detector sensitivity and to incorporate spectral effects of the zone plate, such as its contributions to filtering higher-order radiation. In the ALS microscope, a secondary signal, the current at the front of the OSA, is collected. This signal, which is a convolution of total electron yield and gas ionization yield, serves to correct for instantaneous variations in incident flux (due to beam motion in the storage ring) as well as to correct for the decay in ring current between sample and Io measurements.

Energy scale calibration at the NSLS microscope is routinely carried out by injecting a small amount of CO_2 gas in the He stream bathing the photon path length and recording the sharp Rydberg lines of CO_2 [14,31]. At the ALS, gas and solid reference samples can be recorded for calibration. For this work, the N 1s and O 1s spectra were calibrated with N_2 and O_2, respectively, while the C 1s spectra were calibrated using the known positions of the strong resonances.

Prolonged study of these polyurethane samples results in mass loss of the polyether-rich matrix and selective damage of the carbonyl groups of the PIPA. In both microscopes, after critical analytical measurements such as image sequences, it is routine procedure to monitor the extent of sample damage by recording an image at an energy that shows large spectral changes due to radiation damage (e.g. 289 eV for C 1s studies). Measurements with unacceptably high damage rates are not used in subsequent analysis. The data reported in this work are those recorded before significant damage had occurred ($<5\%$ change).

In the *data analysis* one must evaluate the significance of the derived quantitative results by appropriate statistical and reproducibility tests. The accuracy of the results is limited by the degree to which materials used as reference standards accurately match the chemical character of the components in the material under study. The set of reference compounds must encompass all of the chemical components in the material and the reference spectra should be unaffected by radiation damage or spectroscopic saturation. A large amount of supporting spectroscopy [16–20] has been carried out to make sure spectral features are assigned correctly and that the model spectra are those appropriate to the problem.

3. Results and discussion

3.1. C 1s imaging and spectroscopy: qualitative identification

Prior to the STXM investigation, a different section of the same sample was examined by transmission electron microscopy (Fig. 2). Although the morphology and size distribution of the CPP particles are clearly revealed, TEM imaging of unstained samples cannot distinguish the chemical identity of the individual particles. By contrast, as outlined below, the chemical sensitivity of selective energy imaging NEXAFS microscopy makes identification of the CPP particles very straightforward.

Differences in the X-ray absorption spectra of the components provide the basis for distinguishing PIPA and SAN CPP particles. This is

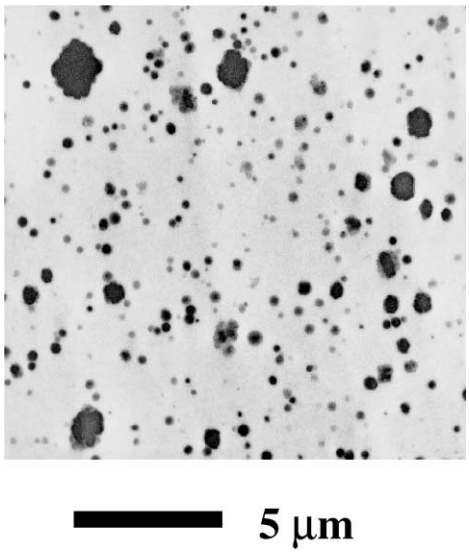

Fig. 2. Transmission electron microscope image of a polyurethane plaque containing a mixture of two types of copolymer polyol (CPP) reinforcing particles. One type is SAN, a copolymer of polystyrene and polyacrylonitrile, and the other type is PIPA, a carbamate-rich polyurethane addition product. *How does one know which particle is which type of CPP*?

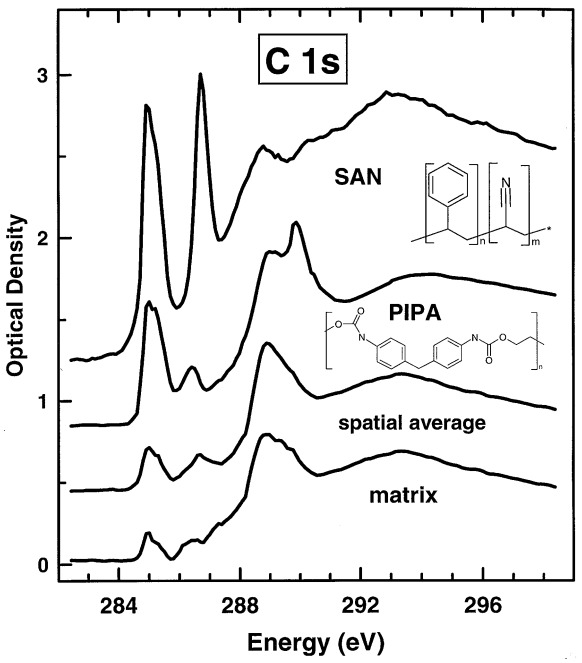

Fig. 3. C 1s X-ray absorption spectra (NEXAFS) of SAN particles, PIPA particles, the polyurethane matrix, and the spatially averaged spectrum of the sample. Vertical offsets of 0.4, 0.8 and 1.2 OD units have been used in plotting the upper three spectra. These spectra were extracted using multi-pixel sums over relevant regions from an image sequence recorded with the scanning transmission X-ray microscope (STXM) at the Advanced Light Source (ALS). The chemical structures indicated for the SAN and PIPA particles are the structural motifs that give rise to the dominant spectral features, but they do not depict all aspects of their structure, which includes polyether components. *What are the values of m and n*?

illustrated in Fig. 3 which plots C 1s NEXAFS spectra of the polyether-rich matrix, the SAN and PIPA particles, along with the average spectrum of the sample. These spectra were acquired at the ALS microscope from the mixed CPP sample using the image sequence mode of acquisition. The SAN spectrum was recorded from an area of $\sim 2\,\mu m^2$ while the PIPA spectrum was recorded from an area of $\sim 0.2\,\mu m^2$. The spectra are similar to those recorded in point-mode from other samples containing larger spatial regions of these CPP materials. The spectra of both PIPA and SAN exhibit a strong low-energy transition at 285 eV, which is associated with C 1s $\rightarrow \pi^*_{C\equiv C}$ transitions at the C–H carbons of the phenyl ring common to both structures. In addition, the SAN particle has a strong transition at 286.7 eV arising from C 1s $\rightarrow \pi^*_{C\equiv N}$ transitions of the acrylonitrile component (AN) of the styrene/acrylonitrile (SAN) copolymer. This feature is unique to the acrylonitrile component of the SAN particles which provides the basis both for distinguishing SAN from PIPA and for quantitative analysis of the styrene/acrylonitrile composition of individual SAN particles. At 287.2 eV, on the high-energy side of the $\pi^*_{C\equiv N}$ peak, the optical density of the PIPA particles and the matrix is the same and very low relative to that for SAN. Thus, an ideal strategy for selective imaging of SAN is to image at 287.2 eV, where the SAN particles are in high contrast but the PIPA particles are indistinguishable from the matrix. Note that the quality of this 'sorting' of the two types of CPP particles depends on making a careful choice of energy, accurate energy calibration, and also on the spectral purity of the imaging photon beam. Any higher order or stray light contamination reduces the chemical contrast. At higher energy, around 288 eV, the

matrix begins to have a very strong absorption associated with the C 1s $\rightarrow \sigma^*_{C-O}$ transitions in the polyether chains. At somewhat higher energy, 289.8 eV, the PIPA particles have a sharp peak associated with C 1s(C=O) $\rightarrow \pi^*_{C=O}$ transitions. In pure PIPA this feature is stronger than the intense 285.1 eV $\pi^*_{C=C}$ peak and it occurs at an energy where SAN does not have a sharp feature. On this basis one might expect 289.8 eV to be an ideal energy for selective imaging of PIPA. However, in practice, while imaging at 289.8 eV gives some relative enhancement of contrast of PIPA relative to SAN, it is an inefficient means to highlight PIPA relative to SAN because of the strong absorption by both the matrix and SAN at this energy which results in poor overall contrast. This energy could be useful for distinguishing PIPA particles from segregated ureas, which absorb at 289.4 for a TDI-based system [23]. In general, it is much easier to see strong absorption against a weak background (as in imaging at 285.1 eV which dramatically highlights both types of reinforcing particles against the weakly absorbing polyurethane matrix) than it is to detect strong absorption against a background of similar absorption strength. As a further example of the relative contrast afforded by $\pi^*_{C\equiv N}$ versus $\pi^*_{C\equiv O}$ transitions, the spatially averaged spectrum (Fig. 3, obtained by summing the spectra from all pixels in the $\sim$100 μm^2 area imaged), gives some indication of the SAN-specific peak at 287 eV but essentially no sign of the PIPA-specific peak at 290 eV. Comparison of the spatially resolved spectra to the spatially averaged spectrum emphasizes the value of good spatial resolution in NEXAFS chemical analysis of heterogeneous materials.

When using variable spectroscopic sensitivity to highlight a specific component, one must be concerned about the effect of density and thickness variations between different phases in the sample, and among different sections of the same sample. These factors can complicate the otherwise straightforward approach of imaging using chemically specific energies derived from model NEXAFS spectra. Density and thickness variations can be compensated by normalization of chemically sensitive images to images measured at photon energies outside of the chemically sensitive near-edge regions.

C 1s NEXAFS microscopy works very well in differentiating the two CPP particles in this sample. Fig. 4 compares images recorded at 285.1 eV ($\pi^*_{C\equiv C}$) and 287.2 eV ($\sim \pi^*_{C\equiv N}$) of a 14 $\mu m \times 14$ μm region of the sample. As discussed above, the energy chosen for the second image was not at the top of the $\pi^*_{C\equiv N}$ resonance peak but rather slightly above, in order to minimize the difference between the absorption by the polyether-rich matrix and the PIPA, so that the SAN particles have the highest contrast. The image at 285.1 eV (Fig. 4a) highlights both types of CPP particles with very strong contrast relative to the polyurethane matrix. This is as expected from the strong $\pi^*_{C=C}$ absorption by the phenyl groups of the aromatic CPP particles and much smaller absorption by the polyurethane matrix, which is polyether rich. It is very clear that imaging at 287.2 eV (Fig. 4b) provides complete selectivity for the SAN particles, based on their acrylonitrile content. Images at 289.8 eV (not shown) provide only limited ability to distinguish the two types of CPP particles. However, the PIPA particles can be readily identified in the difference of the 285.1 and 287.2 eV images, as illustrated in Fig. 4c. We note that careful choice of an acquisition strategy, such as that employed to record the SAN-selective image in Fig. 4b, is preferable to image subtraction as this avoids possible artifacts associated with image drift, image scale changes, etc. Such artifacts give rise to ghost images at the large SAN particles in Fig. 4c, particularly the lower-half of the image, even though every effort was made to match the spatial scales of the two images prior to subtraction. As described in the following section, regression analysis of image sequences using fits of the spectrum at each pixel to spectral standards [29], provides extremely powerful chemical analysis. If the spectral standards are suitable, this approach gives the quantitative chemical composition at each point in the region studied.

3.2. Chemical contrast at the N 1s and O 1s edges

While the C 1s edge clearly provides excellent ability to distinguish these two types of reinforcing

particles, it is also of interest to investigate the chemical contrast at the N 1s and O 1s edges. All of the nitrogen in SAN is at the unsaturated nitrile group (C≡N) whereas the nitrogen in PIPA and the matrix is in essentially saturated environments (N–H). Thus, one might expect very strong selectivity for SAN at the energy of the N 1s $\rightarrow \pi^*_{C\equiv N}$ transition. Similarly, since the SAN particles nominally do not contain oxygen, one might expect strong contrast at the O 1s edge. In spite of the seemingly "obvious" potential for image contrast at these energies, we must remember that the total absorption cross-section at each X-ray energy for a particular component is governed by a number of factors, including density differences, thickness differences and the background from lower energy core/valence absorption edges, in addition to the chemically specific transition.

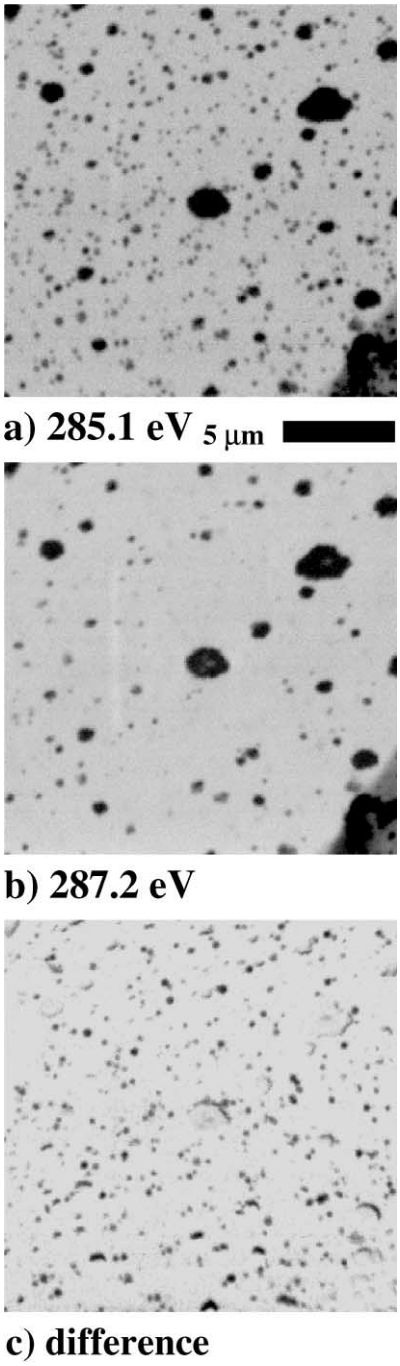

Fig. 4. Comparison of X-ray microscopy images at (a) 285.1 eV and (b) 287.2 eV of a polyurethane containing SAN and PIPA CPP particles recorded with the Stony Brook STXM at the National Synchrotron Light Source (NSLS). (c) Difference of the 285.1 and 287.2 eV images which highlights the PIPA particles only. The ghost signals at the positions of many of the SAN particles are from imperfect registry of the two images. In these transmission images dark regions correspond to higher absorption.

Fig. 5 compares N 1s spectra of the three components, and images recorded with the ALS STXM at several energies in the N 1s spectral region. The contrast in the N 1s region is lower than at the C 1s edge (on account of the large, underlying C 1s signal), except at 399.8 eV (image b), the energy of the strong N 1s $\rightarrow \pi^*_{C\equiv N}$ transition of the nitrile group. Imaging at 399.8 eV preferentially highlights the SAN relative to the PIPA particles and is clearly as effective as C 1s selective energy imaging for particle type identification. The N 1s spectrum of PIPA is very similar to that of the matrix, as expected since all of the matrix nitrogen is in a carbamate environment in this particular polyurethane formulation [20]. Although their spectral shapes are similar, the PIPA particles are somewhat more dense than the matrix. Therefore they have a higher optical density at all energies and they remain visible throughout the whole N 1s region.

Fig. 6 compares O 1 s spectra of the PIPA, SAN and matrix components, along with images recorded with the ALS STXM at the indicated

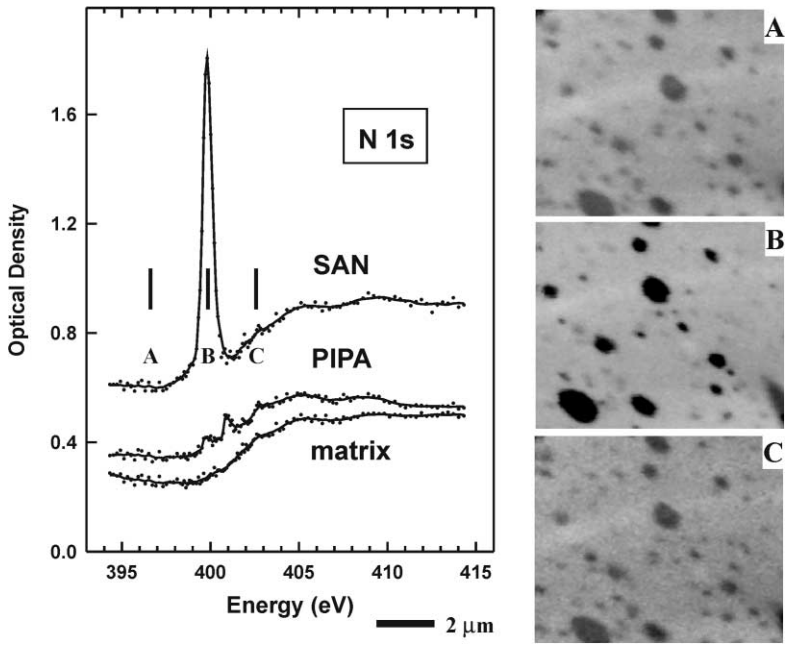

Fig. 5. (left) N 1s spectra of the matrix, PIPA and SAN particles recorded with the ALS STXM in linescan mode. No spectral offsets were used. (right) Transmission mode images recorded at 397, 400 ($\pi^*_{C\equiv N}$) and 403 eV, respectively, in the N 1s region. Note the clear selective identification of the SAN particles in the 400 eV image.

energies. In the O 1s spectral region it is the PIPA particle that has the unique spectral signature, namely the $\pi^*_{C=O}$ resonance at 532.5 eV. While imaging at this energy does highlight the PIPA relative to the SAN particles (PIPA are the darker small particles in Fig. 6b, see arrow), the contrast is relatively low since the O 1s $\rightarrow \pi^*_{C=O}$ transition is a weak feature relative to the remainder of the O 1s signal, in part associated with the polyether content of the PIPA particles but mainly with underlying N 1s and C 1s absorption. Since the chemical structures of both the matrix and PIPA contain oxygen while the nominal structure of SAN does not, we expected the SAN to appear with strong negative contrast in the O 1s region. However, the SAN particles used in this CPP formulation do have some polyether component (as do all copolyol polymer particles, see below) and, therefore, they have an O 1s spectral signature rather similar to the ether signal present in both the PIPA particles and the matrix. The increase in signal across the O 1s edge is only 10% for SAN, much less than the increase for the PIPA and matrix particles. This leads to somewhat lower contrast of SAN in the O 1 s continuum. However, the optical density of the SAN CPP particles remains larger than the surrounding matrix at all energies and thus the expected contrast reversal was not observed. This could be because the SAN particles are thicker than the rest of the section, they have a higher density, or they have a higher absorption cross-section. A higher overall spectroscopic cross section does exist because of the strong N 1 s absorption in SAN. The SAN particles are also known to be more dense that the matrix. Overall, there is relatively weak spectral contrast at the O 1s edge since it is superimposed on the strong C 1s and N 1s continua This limits the ability to differentiate SAN and PIPA particles by means of selective energy imaging at the O 1s edge.

3.3. Particle size analysis

It is clear from Figs. 4–6 that the size distribution of the SAN particles differs from that of the

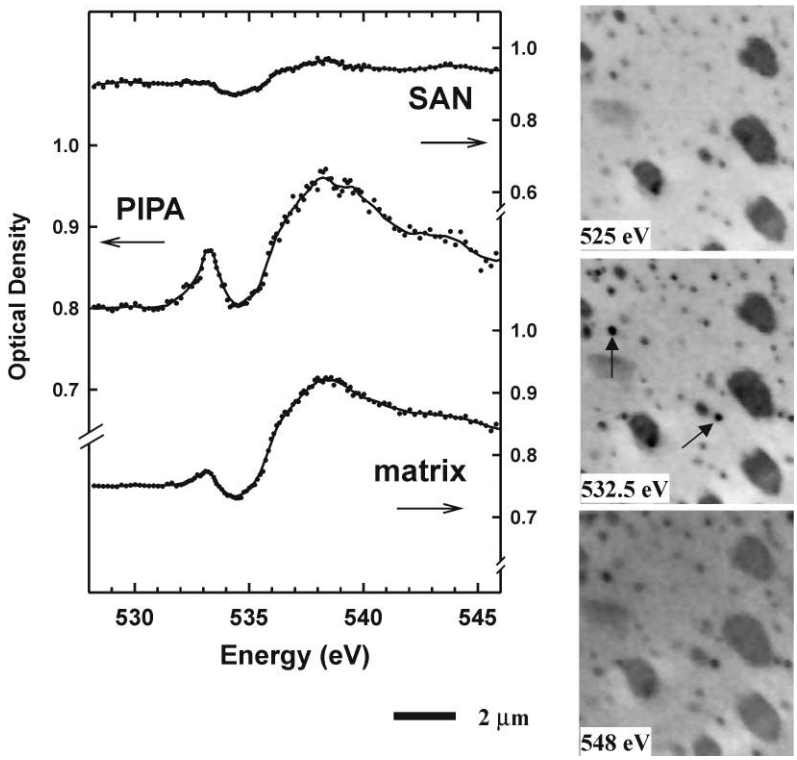

Fig. 6. (left) O 1s spectra of the matrix, PIPA and SAN particles recorded with the ALS STXM in linescan mode. The appropriate OD scales for each species are indicated by arrows. (right) Transmission images recorded at 525, 532.5 ($\pi^*_{C=N}$) and 548 eV respectively, in the O 1 s region. Note the enhanced contrast of the PIPA particles in the 532.5 eV image.

PIPA particles. We have quantitatively analyzed the apparent particle size distributions of each type of CPP particle, based on chemically selective C 1s imaging. (We denote these particle sizes as 'apparent' since the section is much thinner than the diameter of most particles and thus there are artifacts associated with the random sampling of the levels of particles the section was cut through [32]). In addition we have determined the apparent particle size distributions from TEM images, in some cases of exactly the same thin section of the sample that was analyzed by STXM. The particle size analysis was carried out in the following manner. A threshold value corresponding to about 10% greater than the minimum intensity in the particles was applied to the full image to generate a mask image in which each pixel is either black (0) or white (1). The area of each particle was then determined by summing the number of contiguous white pixels. Finally, all particles are assumed to be circular in order to compute the particle diameter from the measured area. Systematic errors of this procedure include: reliability of the thresholding (a range of values was explored and the distributions reported correspond to the best thresholding achievable); occurrence of some particles sectioned through the top or bottom regions rather than the middle; effects of particle curvature which blur the boundaries of the particles; errors associated with finite sampling; non-circular particle cross-sections. The impact of these types of systematic errors on particle size distributions is discussed elsewhere [32].

Histograms of the distributions of the particle sizes (~diameters) derived from the two STXM images recorded at NSLS (Fig. 4) and from multiple ALS STXM and TEM images are shown in Fig. 7. One hundred to several hundred particles

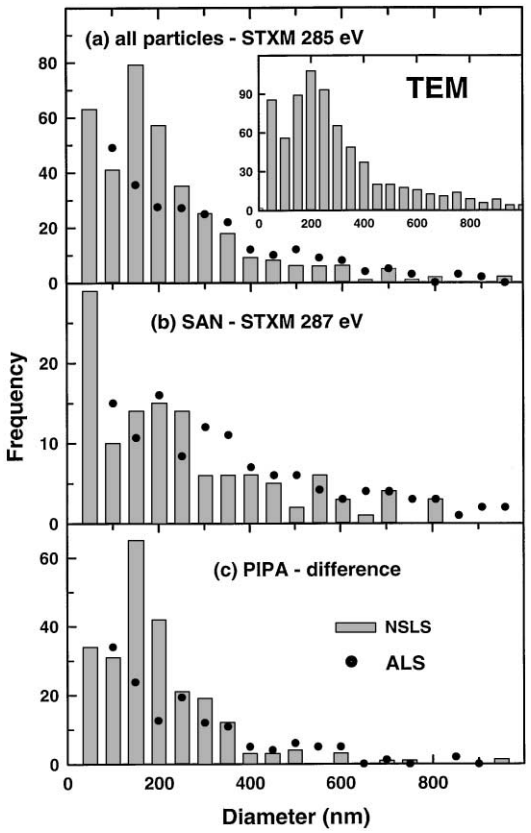

Fig. 7. (a) Histograms of particle sizes derived from STXM images recorded at 285.1 eV at NSLS (image shown in Fig. 4) and at ALS. The inset shows the particle size distribution derived from analysis of four TEM images (total area of $\sim$2000 μm^2, $\sim$400 particles). (b) SAN particle size distribution derived from STXM images recorded at 287.2 eV at NSLS (Fig. 4) and ALS. (c) The difference of the particle size distributions of STXM images at 285.1 and 287.2 eV, which is the PIPA particle size distribution.

in each image were analyzed. Fig. 7a compares the particle size distribution, independent of chemical composition, as measured from STXM images at 285.1 eV (e.g. Fig. 4) and from TEM images. The 285.1 eV STXM and TEM distributions are similar, each exhibiting two maxima – one around 50 nm, the other around 150–200 nm, as well as a long tail to larger size. Fig. 7b is the size distribution of the SAN particles as determined from analysis of 287.2 eV STXM images (Fig. 4). Note the change in vertical scale. The SAN distribution is clearly different. Relative to the average particle size distribution (Fig. 7a), there are more large particles, fewer particles in the middle range, and a relatively large number of sub-100 nm SAN particles. Fig. 7c depicts the particle size distribution of the PIPA particles derived from the difference in the size distributions derived from 285.1 and 287.2 eV STXM images. The PIPA particle distribution is very different from the average distribution, with the PIPA particles having a narrower range of sizes, clustered around 200 nm. This analysis shows that there are very few PIPA particles larger than 0.5 μm, and that the peak of the PIPA distribution lies below 200 nm. In contrast, the SAN particle size distribution is more complicated. The size-weighted average size is around 400 nm. Most SAN particles are smaller than 1 μm and many SAN particles are smaller than 0.1 μm, but there are also a number of SAN particles in the 2–3 μm range. In several cases the larger SAN particles have a 'cauliflower' shape (see Figs. 2 and 4), suggesting they may be agglomerates of smaller particles. Results from the two X-ray microscopes are in good agreement, although the higher spatial resolution of the NSLS microscope allows better definition of the size distributions at small sizes. The power of STXM to partition particle distributions according to chemical composition is well illustrated by this example.

3.4. Composition maps from regression analyses of image sequences

Fig. 8 presents maps of the chemical components of this system – polystyrene (pS), polyacrylonitrile (pAN), polyol, matrix, and PIPA – obtained by a 5-component regression analysis of a sequence of 72 images (12×8 μm) between 280 and 291 eV recorded at the ALS. The indicated grey scales correspond to relative mol% since the model spectra were on absolute oscillator strength per repeat unit scales. The model spectra for the matrix and the PIPA are those plotted in Fig. 3, extracted from regions of this image sequence. The model spectra of polypropylene oxide (analog to the polyol component of the CPP particles), polystyrene (pS) and polyacrylonitrile (pAN) were recorded on un-oriented samples with the Stony

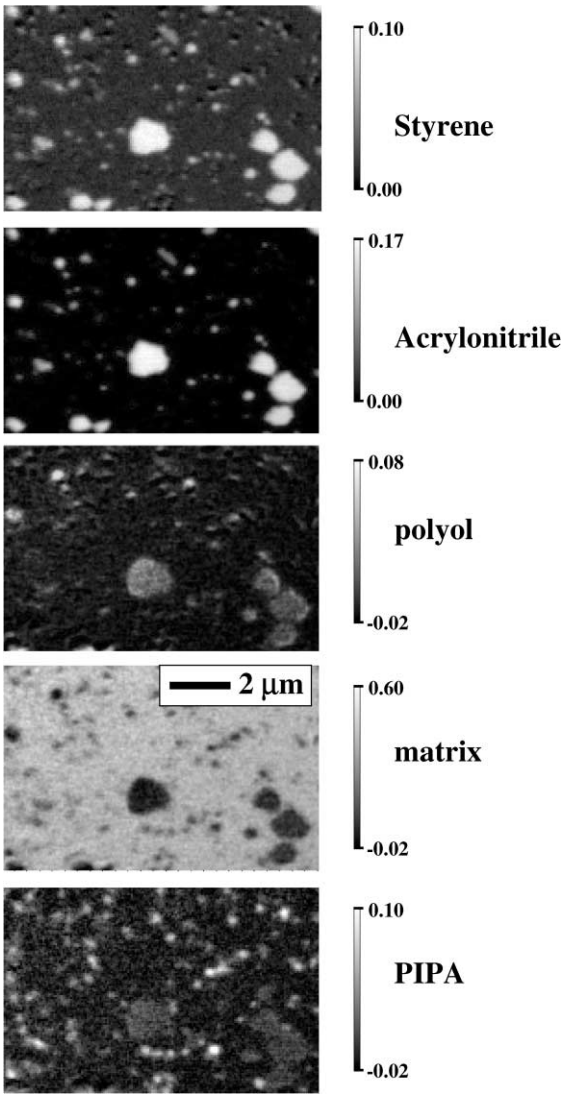

Fig. 8. Component maps for polystyrene, polyacrylonitrile, polyol, polyurethane matrix and PIPA derived from linear regression analysis of the spectrum at each pixel in a C 1s image sequence recorded at the ALS. The portion of the aligned sequence analyzed consisted of 171×111 pixel images (80 nm/pixel) recorded at 72 energies between 280 and 291 eV. See text for details of the models used. The vertical scales indicate relative mol%.

Brook STXM at NSLS using a defocused beam to ensure no radiation damage artifacts. The model spectra from NSLS have been carefully calibrated and the energy resolution matched to that used for the ALS measurements.

The individual component images clearly support the conclusions drawn from selective energy imaging (Fig. 4). In particular, they show that there are both large and small SAN particles but only small PIPA particles. The polyol map shows signal at the SAN and PIPA particles whereas there is negligible signal at the corresponding locations in the matrix map. While there is some overlap with the matrix signal, the very large difference between the matrix and polyol maps indicates that C 1s NEXAFS microscopy is able to distinguish pure polyether–polyol in the CPP particles from the partially aromatic polyurethane matrix despite their strong spectral similarity, which arises since the matrix is predominantly polyether-polyol (see Fig. 3). This differentiation has enabled measurement of the amount of polyether-polyol in the SAN and PIPA particles. The PIPA image identifies and quantifies the PIPA particles. It also shows structure in the matrix, which may be evidence for the hard phase microsegregation intrinsic to aromatic polyurethanes [23]. Further study is needed to verify that point. Finally, the pS map has a weak, diffuse signal in the matrix region which may help explain a discrepancy between the styrene/acrylonitrile ratio measured by STXM and that expected from the formulation. This issue is discussed further in the following section which presents the quantitative results for the CPP particle compositions derived from analysis of the C 1s image sequence.

Fig. 9 presents composition maps derived from image sequences recorded in the N 1s and O 1s spectral regions. Since the N 1s and O 1s spectra of the pure materials were not available, the pS and pAN components were not analyzed separately. Instead, the image sequence was fit to linear combinations of spectra internally generated from selected regions known to be PIPA, SAN and the matrix. The N 1s analysis clearly distinguishes the SAN particles and could readily be used as the basis for quantitation of the acrylonitrile component of SAN. Regression analysis of O 1s image sequences gives reasonable identification of the PIPA particles, but has limited ability to distinguish the SAN from the matrix. The O 1s is the least favorable of the three core edges, which is not surprising given the similarity

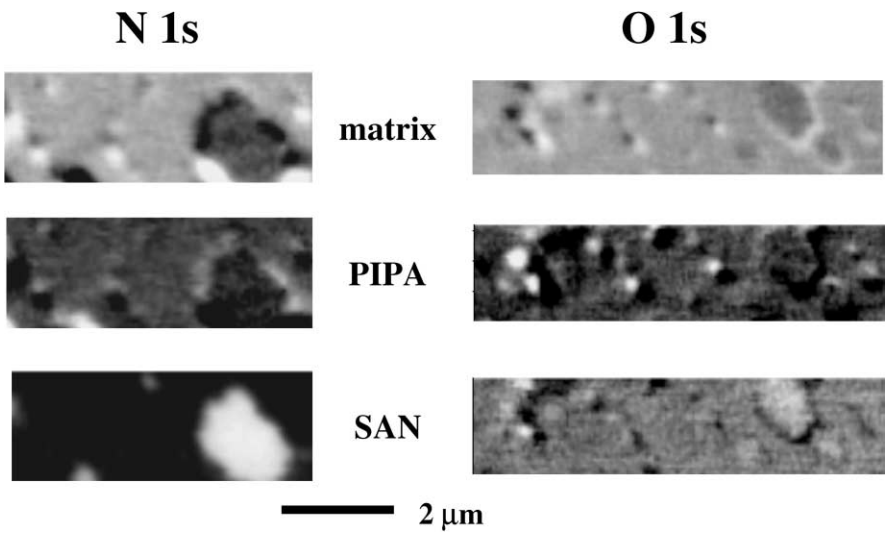

Fig. 9. Component maps for PIPA, SAN and matrix derived from linear regression analysis of the spectrum at each pixel in N 1s and O 1s image sequences recorded at the ALS. In these component maps brighter regions correspond to higher concentration or thickness.

of the O 1s spectra of the three main components (Fig. 6).

3.5. Quantitative compositional analysis of the CPP-reinforcing particles

In addition to identification of different CPP materials, and the qualitative aspects of the compositional mapping, it is possible to generate quantitative chemical compositions from either the component maps or from point spectra [19,20,33–36]. In this section, we describe the use of signals extracted from image sequences to (i) quantify the composition of the two types of reinforcing particles and (ii) to determine the ratio of polystyrene (pS) and polyacrylonitrile (pAN) in several of the larger SAN copolymer particles.

We have used two approaches to the quantitative analysis of the chemical composition of individual reinforcing particles. For both types of particles, the compositions were determined from quantitative component maps derived from the C 1s image sequence (Fig. 8) as outlined below. We have also performed regression analyses of selected PIPA and larger SAN particles by curve fit analysis of spectra extracted by summation over multi-pixel regions from the C 1s image sequence. The compositions determined by spectral curve fit analysis are in good agreement with the results of the image sequence analysis, so only the latter is reported in detail here. In order to establish quantitative intensity scales, the model spectra were background subtracted and converted to an oscillator strength per repeat unit scale, by setting the far C 1s continuum to match the value for atomic carbon [37,38] and then multiplying by the number of carbon atoms per repeat unit – polyether (3), polystyrene (8), polyacrylonitrile (3), and PIPA modeled as MDI reacted with a C4 diol (19). The extracted PIPA and SAN C 1s spectra were then curve fit to find the mixture of the spectra of pure components which best reproduced the spectral shapes in the chemically sensitive 284–291 eV region. An equivalent least-squares minimization procedure was accomplished with the regression analysis of the image sequence from 280 to 291 eV (Fig. 8). With either approach, the derived regression coefficients are the relative mol% values for each species so that normalization to the sum of these values gives absolute mol%. The absolute mol% values were then converted to wt% using the molecular masses of the repeat units – polyether (42), polystyrene (104),

polyacrylonitrile (53), and PIPA modeled as MDI reacted with a C4 diol (278).

Table 1 reports the analysis results from the component mapping for four SAN and four PIPA particles. The quality of the fits to the extracted C 1 s spectra are illustrated in Figs. 10 and 11 for SAN and PIPA, respectively. In both the SAN and PIPA particles there is an appreciable amount of polyether – 12(2) wt% in SAN and ~15(4) wt% in PIPA. The four SAN particles analyzed are all much larger than the thickness of the microtomed thin film – the smallest particle from which compositional numbers were derived is about 0.5 μm diameter, whereas the film was ~0.1 μm thick. Thus the polyether component identified by this quantitative analysis is unlikely to arise from matrix above or below the particle, but rather to be part of the chemical make-up of the particle itself. Since the size of the PIPA particles approaches that of the specimen thickness, this comment is less applicable to the PIPA particles, and thus some of the polyether signal found nominally in the PIPA may be from matrix, either on top or below the PIPA, or even at the edges where it may be partly mixed in on account of the limited spatial resolution. CPP particles are synthesized in polyether polyol in a manner that explicitly forms covalent links to the CPP particles [26]. Thus it is very likely that polyol is incorporated into the CPP particles. Infrared spectroscopic analysis of extracted SAN solid gave an estimate of 10 wt-% incorporated polyol, in reasonable agreement with our analysis. The four large SAN particles in the image sequence which were analyzed were found to have relatively uniform compositions, with a variation of less than 5% in the *ratio* of the styrene to acrylonitrile content. The average weight ratio of (pS) to (pAN) in these larger SAN particles is 0.86(2). Interestingly, this pS/pAN ratio is lower than that predicted from the relative mass of the monomer feedstocks in the bulk formulation of the SAN

Table 1
Quantitative in situ analysis of the chemical composition of individual polyurethane copolymer polyol-reinforcing particles

	Mol%[a]				Wt%[b]			
#	E[c]	S[c]	AN[c]	S/AN[c]	E[c]	S[c]	AN[c]	S/AN[c]
A. SAN particles (see Fig. 10)								
1	21	25	54	0.45	14	40	46	0.88
2	18	25	57	0.45	12	40	48	0.85
3	16	25	59	0.43	11	40	49	0.82
4	22	24	54	0.45	14	40	46	0.88
B. PIPA particles (see Fig. 11)								
	Mol%[a]		Wt%[b]					
#	C[c]	E[c]	C[c]	E[c]				
1	49	51	86	14				
2	40	60	81	19				
3	70	30	94	6				
4	66	34	92	18				

[a] Based on regression analysis of the C 1s image sequence (Fig. 8) using model spectra whose vertical scales had been established on a per-repeat-unit oscillator strength basis. The estimated error based on the quality of the fits is ±3 mol% {this does not account for systematic errors associated with mismatch of models and the material under study} The quality of the fits are illustrated in Figs. 10 and 11. Results for four particles are presented to indicate reproducibility of the analysis and uniformity of the composition of the particles. While the fit was made to five components (polyurethane matrix, pure polyol, polystyrene, polyacrylonitrile and PIPA), the table reports the compositions of the main components for each particle type, ignoring the minority components which contribute a few % to the fit.

[b] Wt% (a) = mol% (a) * mw (a)/(Σ_i mol%$_i$ * mw$_i$) where mol% (a) is mol% of species *a* and mw$_i$ represents the molecular weight of species *i*.

[c] E = polyether, S = polystyrene, AN = polyacrylonitrile, C = carbamate (PIPA)

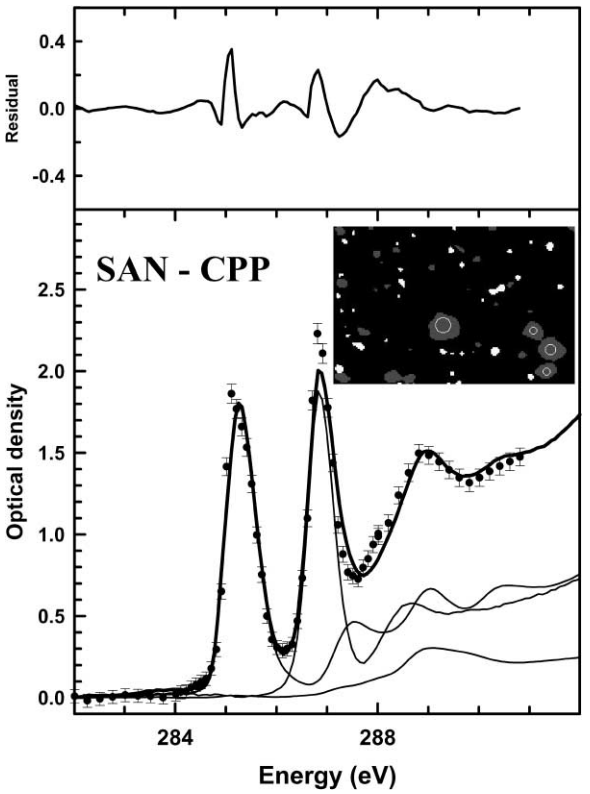

Fig. 10. Illustration of the quality of the C 1s image sequence curve fit analysis summed over four SAN particles. The dots are the spectral data summed over ~1000 pixels, the solid line is the fit, and the thin solid line indicates the pS, pAN and polyol component contributions. The circles superimposed on the four SAN particles in the inset image indicate the regions of the sample from which this spectrum was derived. This navigation image was derived from the SAN and PIPA component maps (Fig. 8) by thresholding to have 0/1 coded maps which were summed with a 1 : 3 weighting.

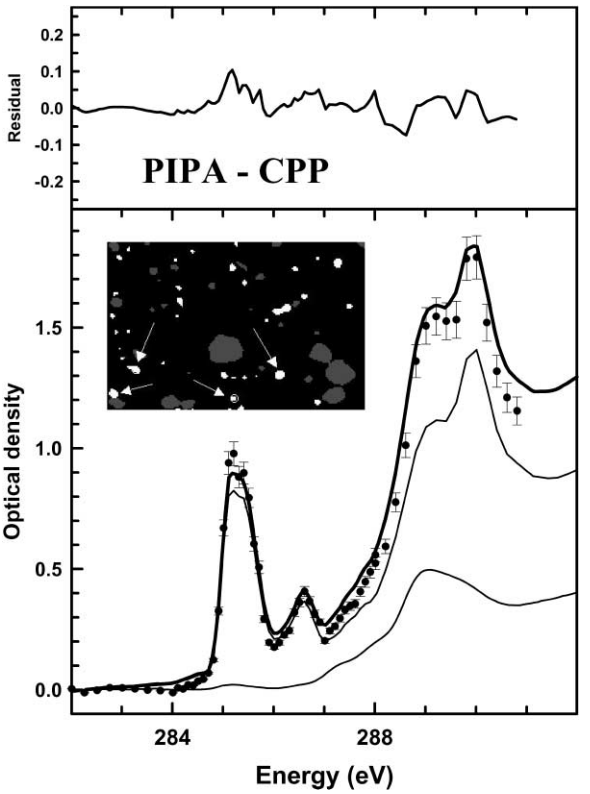

Fig. 11. Illustration of the quality of the C 1s image sequence curve fit analysis summed over four PIPA particles. The dots are the spectral data summed over ~200 pixels, the solid line is the fit, and the thin solid lines indicates the carbamate and polyol component contributions. The four PIPA particles analyzed are indicated in the inset navigation image (see caption to Fig. 10).

particles, which corresponds to a pS to pAN wt% ratio of 1.50. The reason for this discrepancy is not fully understood at present. One possibility is incomplete polymerization of the styrene during formation of the CPP-polyol. Unreacted styrene monomer or polystyrene oligimer could then be preferentially located in the polyurethane matrix relative to the amount in the SAN particles. A low level of signal is observed in the polystyrene component map (Fig. 8) throughout the matrix region which provides qualitative support for this interpretation.

These results illustrate the ability of STXM-based NEXAFS microscopy to provide quantitative chemical analysis on submicron regions with better than 5% precision. Other examples of quantitative polymer analysis with STXM include: urea/urethane composition in model polyurethanes [6,19] and high water content polyurethanes [23]; polystyrene/poly(methyl meth-acrylate) blends [35], PS, Br-PS thin film structures [36], and confinement structures [39]. The level of precision demonstrated in this work should be achievable whenever there are characteristic spectral signatures of the individual components and the radiation damage rates are low enough to allow acquisition of representative images and spectra. Aided by

image sequence procedures, it is possible to carry out this level of detailed analysis on features down to and even slightly smaller than 0.1 μm in diameter.

4. Summary

Based on its spectroscopic and imaging capabilities, scanning transmission X-ray microscopy (STXM) has been shown to be a suitable tool for distinguishing polymer-reinforcing particles of different chemical composition, and for quantifying their chemical composition and size distributions. Comparisons of images at selected energies provide a quick and reliable means to differentiate SAN and PIPA CPP particles. The C 1 s region is better than the N 1s or O 1s regions, partly because of better intrinsic spectral resolution (smaller natural linewidths), but also because the contrast at the C 1s edge is much higher since there is negligible underlying background continuum. N 1s imaging at 400 eV also provides high selectivity. Quantitative spectral analysis showed that both types of CPP reinforcing particles contain ~15 wt% polyether polyol. The presence of this component in the SAN particles leads to relatively poor ability to differentiate SAN and PIPA particles at the oxygen edge. The polystyrene/polyacrylonitrile ratio in large SAN particles was determined to be constant within the precision of the measurements. This study is a good illustration of the power of soft X-ray spectromicroscopy for quantitative microanalysis of soft, radiation sensitive materials such as polymers and biological specimens. It is one of many possible areas of application of soft X-ray spectromicroscopy to polymer science.

Acknowledgements

The authors thank Gene Young for assistance with sample preparation, and Dana Gier and Mark Adams for helpful discussions. We thank Dr. Chris Jacobsen (SUNY Stony Brook) for generously sharing his image ('stack') data acquisition and analysis software, and Eric Kneedler for supplying the core of the image-spectra regression analysis code. Data was recorded using the Stony Brook STXM at the X-1A NSLS beamline and the BL7.0 STXM at ALS. The Stony Brook STXM was developed by the groups of J. Kirz and C. Jacobsen, with support from the Office of Biological and Environmental Research, US DOE under contract DE-FG02-89ER60858, and the NSF under grant DBI-9605045. The zone plates were developed by S. Spector and C. Jacobsen of Stony Brook and Don Tennant of Lucent Technologies Bell Labs, with support from the NSF under grant ECS-9510499. The ALS STXM was developed by T. Warwick (ALS), B. Tonner (UWM) and collaborators, with support from the US DOE under contract DE-AC03-76SF00098. Zone plates at ALS were provided by Eric Anderson of CXRO, LBNL. H. Ade, S.G. Urquhart, and A.P. Smith are supported by NSF Young Investigator Award (DMR-9458060) and by Dow Chemical. We thank Pierre Brassard for use of his particle size analysis program in early studies. A.P. Hitchcock's work is supported by NSERC research and strategic grants.

References

[1] D.R. Gier, R.E. O'Neill, M.R. Adams, R.D. Priester Jr., W.A. Lidy, E.G. Rightor, C.G. Barnes, B.L. Davis (Eds.), Filler, Hard Phases and Copolymer Polyols – Their Different Mechanisms to Reinforce Flexible Polyurethane Foams, Proceedings of the Society of Plastics Institute 1998, Dallas, TX.
[2] L.M. Brown, C.A. Walsh, A. Dray, A.L. Bleloch, Microsc. Microanal. Microstruct. 6 (1995) 121.
[3] R. Egerton, Electron Energy Loss Spectroscopy, Plenum Press, New York, 1986.
[4] H. Ade, X. Zhang, S. Cameron, C. Costello, J. Kirz, S. Williams, Science 258 (1992) 972.
[5] H. Ade, B. Hsiao, Science 262 (1992) 1427.
[6] H. Ade, A. Smith, S. Cameron, R. Cieslinski, C. Costello, B. Hsiao, G.E. Mitchell, E.G. Rightor, Polymer 36 (1995) 1843.
[7] A.P. Smith, H. Ade, Appl. Phys. Lett. 69 (1996) 3833.
[8] J. Kirz, C. Jacobsen, M. Howells, Quart. Rev. Biophysics 33 (1995) 33.
[9] H. Ade, in: J.A.R. Samson, D.L. Ederer (Eds.), Experimental Methods in the Physical Sciences, Vol. 32, Academic Press, New York, 1998, p. 225.

[10] C. Jacobsen et al., Proceedings of the International Conference on X-ray and Optical Microanalysis Institute of Physics, Bristol, 1993.
[11] D. Sayre, H.N. Chapman, Acta Crystallogr. A 51 (1995) 237.
[12] T. Warwick, H. Padmore, H. Ade, A.P. Hitchcock, E.G. Rightor, B. Tonner, J. Electron Spectrosc. 84 (1997) 85.
[13] T. Warwick, K. Franck, J.B. Kortwight, G. Meigs, M. Moronne, S. Myneni, E. Rotenberg, S. Seal, W.F. Steele, H. Ade, A. Garcia, S. Cerasari, J. Denlinger, S. Hayakawa, A.P. Hitchcock, T. Tyliszczak, E.G. Rightor, H.-J. Shin, B. Tonner, Rev. Sci. Inst. 69 (1998) 2964.
[14] H. Ade, A.P. Smith, H. Zhang, B. Winn, J. Kirz, E. Rightor, A.P. Hitchcock, J. Electron Spectrosc. 84 (1997) 53.
[15] E.G. Rightor, A.P. Hitchcock, H. Ade, R.D. Leapman, S.G. Urquhart, A.P. Smith, G. Mitchell, D. Fischer, H.J. Shin, T. Warwick, J. Phys. Chem. B 101 (1997) 1950.
[16] S.G. Urquhart, A.P. Hitchcock, R.D. Leapman, R.D. Priester, E.G. Rightor, J. Polym. Science B: Polym. Phys. 33 (1995) 1593.
[17] S.G. Urquhart, A.P. Hitchcock, R.D. Priester, E.G. Rightor, J. Polym. Sci. B: Polym. Phys. 33 (1995) 1603.
[18] S.G. Urquhart, A.P. Hitchcock, A.P. Smith, H. Ade, E.G. Rightor, J. Phys. Chem. B 101 (1997) 2267.
[19] S.G. Urquhart, A.P. Smith, H. Ade, A.P. Hitchcock, E.G. Rightor, W. Lidy, J. Phys. Chem. B. 103 (1999) 4603.
[20] S.G. Urquhart, A.P. Hitchcock, A.P. Smith, H. Ade, W. Lidy, E.G. Rightor, G.E. Mitchell, J. Electron Spectrosc. 100 (1999) 119.
[21] A.P. Hitchcock, S.G. Urquhart, E.G. Rightor, W. Lidy, H. Ade, A.P. Smith, T. Warwick, Microsc. Microanal. 3 (S-2) (1997) 909.
[22] A.P. Hitchcock, S.G. Urquhart, E.G. Rightor, W. Lidy, H. Ade, A.P. Smith, T. Warwick, Microsc. Microanal. 5 (S-2) (1998) 808.
[23] E.G. Rightor, G.E. Mitchell, S.G. Urquhart, A.P. Smith, H. Ade, A.P. Hitchcock, in preparation.
[24] K. Picken, Urethanes Technology, June 1984 p. 23.
[25] T. Narayan, J.T. Paton, US Patent 4,326,043 to BASF Wyandotte Corp. April 20, 1982. (ref 2.78 of Herrington, cited p. 2.14).
[26] R. Herrington, Flexible Polyurethane Foams, 2nd edition, The Dow Chemical Company, Midland, MI, 1997.
[27] C. Jacobsen, S. Wirick, G. Flynn, C. Zimba, J. Microsc. 197 (2000) 173.
[28] T. Coffrey, M.Sc. Thesis, NCSU, 1998.
[29] A.P. Hitchcock, I. Koprinarov and R. Kneedler, in preparation.
[30] H. Ade et al., Proceedings of VUV-10, World Scientific, Singapore, 1993.
[31] A.P. Smith, T. Coffey, H. Ade, in: J. Thieme, G. Schmahl, E. Umbach, D. Rudolph (Eds.), X-ray Microscopy and Spectromicroscopy, Springer, Berlin, 1998.
[32] J.C. Russ, Computer-Assisted Microscopy: The Measurement and Analysis of Images Plenum Press, New York, 1990.
[33] G.E. Mitchell, et al. 1998 Compendium of ALS Abstracts, LBNL Pub 43431, 1999, p. 282.
[34] G.E. Mitchell, L.R. Wilson, M.T. Dineen, S.G. Urquhart, F. Hayes, E.G. Rightor, A. Hitchcock, H. Ade, Science (2000), submitted for publication.
[35] H. Ade, D.A. Winesett, A.P. Smith, S. Qu, S. Ge, S. Rafailovich, J. Sokolov, Europhys. Lett. 45 (1999) 526.
[36] H. Ade, D.A. Winesett, A.P. Smith, S. Anders, T. Stammler, C. Heske, D. Slep, M.H. Rafailovich, J. Sokolov, J. Stöhr, Appl Phys. Lett. 73 (1998) 3773.
[37] B.L. Henke, P. Lee, T.J. Tanaka, R.L. Shimabukuro, B.K. Fujikawa, Atom. Nucl. Data Tables 27 (1982) 1.
[38] A.P. Hitchcock, D.C. Mancini, J. Electron. Spectrosc. 67 (1994) 1.
[39] S. Zhu, Y. Liu, M.H. Rafailovich, J. Sokolov, D. Gersappe, D.A. Winestt, H. Ade, Nature 400 (1999) 49.